Available online at www.sciencedirect.com

SCIENCE DIRECT®

European Journal of Mechanics B/Fluids ●●● (●●●●) ●●●–●●●

Secondary instability mechanisms in the wake of a flat plate

Stéphanie Julien [a], Sabine Ortiz [a,b,*], Jean-Marc Chomaz [a]

[a] *LadHyX – CNRS, École polytechnique, 91128 Palaiseau, France*
[b] *UME/DFA, ENSTA, chemin de la Hunière, 91761 Palaiseau cedex, France*

Received 25 April 2003; accepted 28 July 2003

Abstract

We extend the work of Sutherland and Peltier (Phys. Fluids 6 (1994) 1267) and investigate numerically the three-dimensional (3D) secondary stability of a wake forming behind a thin flat plate. The primary flow is a Kármán vortex street numerically computed from the two-dimensional (2D) even instability of a parallel wake based on the Bickley velocity profile. Considering the symmetries of the von Kármán Street, the 3D modes are classified into two families, whether symmetric or antisymmetric. For each family, we determine the leading eigenmodes using a Krylov method. The growth rate curves show that both the most unstable symmetric and antisymmetric modes are stationary and present a maximum of amplification for a wavelength of the order of the primary vortex spacing. The maximum growth rate, corresponding wavelength and cutoff wavelength are well predicted by the elliptic instability of the vortex core. The eigenmode structure of the most unstable wavenumber is centered in the core and is typical of the elliptic instability. The hyperbolic instability of the braid region gives a growth rate five times larger and a cutoff two times higher than the ones computed. As recently discussed for mixing layers by Caulfield and Kerswell (Phys. Fluids 12 (5) (2000) 1032), this is not surprising since the hyperbolic instability applies for an unbounded hyperbolic flow. When the region of hyperbolic flow is bounded, intense transient growth is generated, but when time goes to infinity, the instability becomes small or even dies out. Finally, good qualitative and quantitative agreement is found with the experiments previously done by Julien, Lasheras and Chomaz (J. Fluid Mech. 479 (2003) 155) on the secondary instability in the wake of a flat plate for the symmetry selection, the most amplified wavenumber and growth rate.

Keywords: Secondary instability; Wakes; Hyperbolic instability; Elliptic instability

1. Introduction

Wakes, jets or mixing layers have an initial velocity profile with an inflection point and are unstable to two-dimensional (2D) perturbations (Drazin and Reid [1]). As this primary Kelvin–Helmholtz instability develops, the initial vorticity rolls up, leading to the formation of vortices transverse to the flow. This primary state is itself unstable to a variety of either 2D perturbations, as for example the pairing instability of the mixing layer, or three-dimensional (3D) instabilities that often lead to the development of an array of counter-rotating longitudinal (also called streamwise) vortices and to the waviness of the primary vortices. This secondary 3D instability was observed in mixing layers (Browand and Troutt [2], Breidenthal [3], Jimenez [4], Bernal and Roshko [5] and others), in axisymmetric jets, where this instability led mainly to radial ejections of fluid in lateral secondary jets (Yule [6]), in 2D jets (Monkewitz et al. [7]) and in wakes (Meiburg and Lasheras [8], Williamson [9,10], Leweke and Williamson [11]). Two main physical mechanisms have been proposed to explain the development of these 3D secondary flows: the hyperbolic instability of the highly strained region between vortices (see Caulfield and Kerswell [12]) and the elliptic instability of the primary vortices due to the destabilization of Kelvin waves in the vortex core (see Kerswell [13] for a review).

---

[*] Corresponding author.
E-mail address: ortiz@ladhyx.polytechnique.fr (S. Ortiz).

0997-7546/$ – see front matter © 2003 Elsevier SAS. All rights reserved.
doi:10.1016/j.euromechflu.2003.07.001

Pierrehumbert and Widnall [14] in their numerical stability analysis of the Stuart mixing layer [15] showed that the ellipticity of the primary vortices was responsible for the development of 3D modes mostly intense in the vortex core. However, recent stability analysis of mixing layer flows (Klassen and Peltier [16], Potylitsin and Peltier [17] and Caulfield and Peltier [18]) showed that the strong strain, in the so-called braid region separating two consecutive primary vortices, amplified perturbations and ultimately led to the formation of the counter-rotating streamwise vortices. The present paper analyses the respective role of the hyperbolic and the elliptic region in the stability of a numerically computed steady von Kármán street in a streamwise periodic domain. It extends the earlier work of Sutherland et al. [19] who showed that the symmetric and the antisymmetric modes had a similar maximum growth rate, reached at a similar value of the wavenumber. By a systematic study, we show that the elliptic instability imposes the growth rate of the unstable mode for all longitudinal wavenumbers k, whereas the hyperbolic instability determines the localisation of the eigenmode. This somehow surprising result is shown to be linked to the fact that finite hyperbolic regions are responsible for intense transient growth but cannot sustain long time perturbation energy growth as discussed in Caulfield and Kerswell [12]. The agreement with experiments validates the assumption that the interaction with the flat plate plays no role in the 3D instabilities of the “real” spatially developing wake and that all the instability characteristics derive solely from the local property of the flow.

2. The 2D basic flow: the Kármán vortex street

Since no exact solution of the Navier–Stokes equations modelling a Kármán street is known, the basic flow is obtained by direct numerical simulation. Experimentally, Julien, Lasheras and Chomaz [20] showed that the velocity profiles measured at the trailing edge of a thin flat plate are well fitted by the Bickley wake profile:

$$U(\mathrm{y}) = \overline{U} - \frac{\Delta\overline{U}}{1+\sinh^2(y/\delta)}, \tag{1}$$

with δ the bickley wake thickness and $\Delta\overline{U}$ the velocity defect. In the experiments, $\Delta\overline{U}$ was such that $\Delta\overline{U} = 0.8\overline{U}$, $\overline{U}$ being the velocity of the free stream.

The 2D wake, issuing from the spatial evolution of this flow, is therefore characterized by two main parameters, the Reynolds number based on the initial velocity defect and wake thickness, $Re = \Delta\overline{U}\delta/\nu$, ν being the viscosity of the fluid and the Strouhal number $St = \delta f/\overline{U}$ where f is the two-dimensional frequency of the vortex street of the primary vortex sheet. The frequency f is equal to $(2\pi/\lambda_{2D})V$, λ_{2D} being the imposed 2D wavelength and V the phase velocity of the primary vortex. According to the values obtained in the experiments [20], the Strouhal number is equal to $St = (2\pi/5)\delta/\lambda_{2D}$. Since the wake behind a thin flat plate develops spatially very slowly, it can be considered homogeneous in space, when the secondary instability appears. Furthermore, the trailing edge of the plate is far from the 3D mode development and interaction with boundary layers may be neglected. This observation legitimates the use of a temporal stability analysis of a periodic flow to interpret the 3D instability of the flat plate wake instead of the full spatio-temporal analysis of a spatially evolving flow as done for the cylinder wake by Barkley and Henderson [21].

2.1. Computation of the 2D von Kármán street

The basic flow is obtained by a saturation of small initial perturbations of a Bickley wake profile in a streamwise periodic domain in x, with a period corresponding to one wavelength λ_{2D}. The evolution of the 2D velocity, vorticity and pressure perturbations, $\mathbf{u_b}(x,y,t)$, $\boldsymbol{\omega_b} = \omega_b(x,y,t)\mathbf{e_z} = \nabla\wedge\mathbf{u_b}$ and $p_b(x,y,t)$, are governed by the non-linear 2D Navier–Stokes equations:

$$\begin{cases} \operatorname{div}\mathbf{u_b} = 0, \\ \dfrac{\partial\mathbf{u_b}}{\partial t} + \boldsymbol{\Omega}\wedge\mathbf{u_b} + \boldsymbol{\omega_b}\wedge\mathbf{U} + \boldsymbol{\omega_b}\wedge\mathbf{u_b} = -\nabla\left[p_b + \mathbf{u_b}\cdot\mathbf{U} + \dfrac{\mathbf{u_b^2}}{2}\right] + \nu\Delta\mathbf{u_b}, \end{cases} \tag{2}$$

where ν is the numerical viscosity, $\mathbf{U} = U(\mathrm{y})\mathrm{e_x}$ the parallel basic flow velocity given by Eq. (1) and $\boldsymbol{\Omega} = -\frac{\mathrm{d}}{\mathrm{dy}}U(\mathrm{y})\mathbf{e_z}$ the basic flow vorticity. The symmetry of the von Kármán street is imposed and the diffusion of the basic flow is compensated by a body force (Drazin and Reid [1]). This explains the omission of the viscous term $\nu\Delta\mathbf{U}$ in Eq. (2).

The integration procedure is based on a pseudo-spectral method in Cartesian coordinates with periodic boundary conditions in the x and y directions. The x-length sets the periodicity of the von Kármán street to λ_{2D} and the y-length is equal to $4 * \lambda_{2D}$, wide enough to avoid confinement effects.

In the remaining part of the section, we will outline the main steps of the numerical method (see Brancher, Chomaz and Huerre [22] for details and validations of the numerical code). The velocity, vorticity and pressure perturbations are expressed in Fourier space:

$$[\mathbf{u_b}, \omega_b, p_b](x, y, t) = \int\int [\hat{\mathbf{u}}_\mathbf{b}, \widehat{\omega}_b, \hat{p}_b](k_x, k_y, t) * \mathrm{e}^{\mathrm{i}(k_x x + k_y y)} \mathrm{dk_x}\, \mathrm{dk_y}, \tag{3}$$

where k_x and k_y, which belong respectively to $[-\pi/\lambda_{2D}, \pi/\lambda_{2D}]$ and $[-\pi/(4\lambda_{2D}), \pi/(4\lambda_{2D})]$, are the components of the wavevector $\mathbf{k_t} = (\mathrm{k_x}, \mathrm{k_y})$.

In spectral space, the non-linear Navier–Stokes equations, Eq. (2), become:

$$\begin{cases} \mathbf{k_t} \cdot \hat{\mathbf{u}}_\mathbf{b} = 0, \\ \dfrac{\partial \hat{\mathbf{u}}_\mathbf{b}}{\partial t} = P(\mathbf{k}_t)\big[\widehat{\mathcal{F}_{NL}}\big] - \nu \mathbf{k}_\mathbf{t}^2 \hat{\mathbf{u}}_\mathbf{b}, \end{cases} \tag{4}$$

where $P(\mathbf{k_t})$ is the projection operator on the space of the solenoidal field, $Pij = \delta ij - k_i k_j / \mathbf{k_t^2}$ and where $\mathcal{F}_{NL}$ is equal to $\mathbf{u_b} \wedge \boldsymbol{\Omega} + \mathbf{U} \wedge \boldsymbol{\omega_b} + \mathbf{u_b} \wedge \boldsymbol{\omega_b}$.

The advection term $\mathcal{F}_{NL}$ is evaluated in the physical space. The viscous term is calculated exactly, the classical $2/3$ truncation being applied for dealiasing. Time integration is performed with the second-order finite-difference Adams–Bashforth numerical scheme.

The value of the Reynolds number chosen for the simulations corresponds to the experiment of Julien et al. [20] $Re = 220$. The Strouhal number $St = 0.07$ corresponds to that of the linearly most unstable even mode [23]. The numerical viscosity ν is therefore equal to 0.013 and the 2D wavelength λ_{2D} is equal to 2π. For the Bickley profile defined in the simulations, we choose the one-mode of the family of velocity profiles used by Monkewitz [24] to model bluff body wakes. That means $\Delta \overline{U}$ is equal to 2.0 and δ to $1/\sinh^{-1}(1)$ in Eq. (1). The Cartesian mesh is made of 128×512 collocation points, that corresponds to a mesh size in the x and y directions equal to $\delta_x = \delta_y = 0.0491$. The time step is set to $\delta_t = 0.001$, which is small enough for the convergence of the simulation and for the Courant–Friedrish–Levy condition to be satisfied.

At each step of the simulation, we impose the symmetries of the even (sinuous) mode of instability of the Bickley velocity profile (see Drazin and Howard [23]):

$$[\mathrm{u_{bx}}, \mathrm{u_{by}}](\mathrm{x}, \mathrm{y}, \mathrm{t}) = [\mathrm{u_{bx}}, -\mathrm{u_{by}}]\left(\mathrm{x} + \frac{\lambda_{\mathrm{2D}}}{2}, -\mathrm{y}, \mathrm{t}\right). \tag{5}$$

The velocity perturbations are initialized by a modulation in the x-direction of the basic velocity profile (Eq. (1)), satisfaying the symmetries of Eq. (5):

$$\mathrm{u_{bx}}(\mathrm{x}, \mathrm{y}, 0) = -0.01 \cos\left(\frac{2\pi}{\lambda_{\mathrm{2D}}}\mathrm{x}\right) \frac{\mathrm{d}}{\mathrm{dy}} \mathrm{U}(\mathrm{y}), \tag{6}$$

$$\mathrm{u_{by}}(\mathrm{x}, \mathrm{y}, 0) = 0.01 \frac{2\pi}{\lambda_{\mathrm{2D}}} \sin\left(\frac{2\pi}{\lambda_{\mathrm{2D}}}\mathrm{x}\right) \mathrm{U}(\mathrm{y}). \tag{7}$$

2.2. The 2D Kármán street development

Fig. 1(a) shows the evolution of the perturbation energy E as a function of time on a semi-logarithm scale. The kinetic energy E is defined by:

$$E = \iint \mathbf{u_b} \mathbf{u_b}\, \mathrm{dx}\, \mathrm{dy}, \tag{8}$$

integrated over the whole computational domain.

The energy increases exponentially, oscillates and saturates, while the vorticity rolls up and ultimately leads to a steady flow, made of two staggered counter-rotating vortices (Fig. 1(b)). These vortices are strongly deformed when interacting with their neighbours and the total strain rate ε_B, computed using the total velocity field $\mathbf{U_B} = \mathrm{u_b} + \mathbf{U}$, is equal to 0.14 at the vortex center of two staggered rows. The total voticity $\Omega_B = \Omega + \omega_b$, at time $t = 1000$, is plotted on Fig. 1(b). Fig. 1(c) shows the field $\Delta^2 = \varepsilon_B^2 - \Omega_B^2$. As we will recall in the discussion, when Δ^2 is positive (in white on Fig. 1(c)), the flow is locally unstable to hyperbolic instability and the local growth rate is equal to Δ. The maximum value of Δ is 0.47 and is reached at the hyperbolic point of the flow marked by a star on Fig. 1(c). Conversely, negative values of Δ^2 are associated with the core of the vortices (in black on Fig. 1(c)) and are locally unstable to elliptic instability. The variation of energy beween $t = 900$ and $t = 1000$ is of order 10^{-5}. The basic state is stationary in a particular frame that moves at a velovity V. This velocity is precisely determined by minimizing the total advection term $\mathcal{F}_{NL}$ and V is close to 1.29.

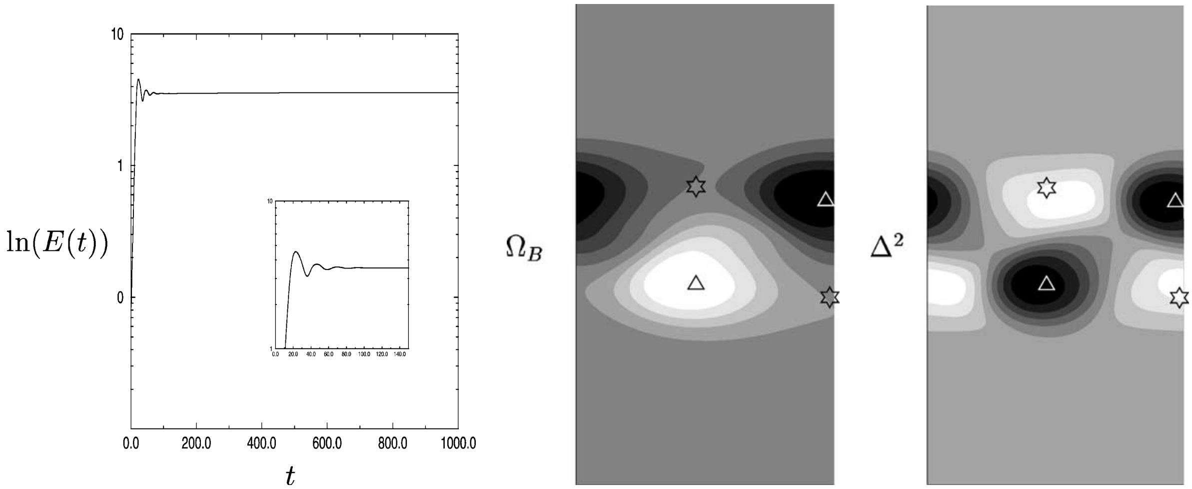

(a) (b) (c)

Fig. 1. (a) Time evolution of the energy for a 2D even perturbation of a Bickley wake at $Re = 220$ and $St = 0.07$; (b) Total vorticity field $\Omega_B = \omega_b + \Omega$ corresponding to the von Kármán street obtained at time $t = 1000$; (c) corresponding field $\Delta^2 = \varepsilon_B^2 - \Omega_B^2$ where ε_B is the local strain rate. The maximum vorticity (marked by a triangle) is 0.55 and the maximum value of Δ is 0.47 (marked by a star). The isocontours are equally spaced. Core regions are unstable to elliptic instability and correspond to negative values of Δ^2 (in black) whereas positive value of Δ^2 (in white) are obtained in the braid regions, locii of the hyperbolic instability.

3. Linear three-dimensional stability analysis of the Kármán street

We investigate numerically the three-dimensional instability of the periodic wake plotted on Fig. 1(b), via a fifth order Krylov method (Edward et al. [25]). This procedure differs from the study of Sutherland and Peltier [19] who investigated the 3D stability of the flow during the roll-up of the vorticity, whereas we added a body force to cancel the diffusion of the Bickley profile and waited long enough for the von Kármán street to become stationary to a very high precision. In Sutherland and Peltier [19], the growth rates of the primary and secondary instabilities are of the same order and the results are delicate to interpret since the quasi steady approximation is not fulfilled.

The 3D Navier–Stokes equations (Eq. (9)) are linearized around the basic state which is the saturated Kármán street plotted on Fig. 1(b), and characterized by the total velocity $\mathbf{U_B}$ and total vorticity $\boldsymbol{\Omega_B}$:

$$\begin{cases} \operatorname{div}\tilde{\mathbf{u}} = 0, \\ \dfrac{\partial \tilde{\mathbf{u}}}{\partial t} + \boldsymbol{\Omega_B} \wedge \tilde{\mathbf{u}} + \tilde{\boldsymbol{\omega}} \wedge \mathbf{U_B} = -\nabla\left[\tilde{p} + \tilde{\mathbf{u}} \cdot \mathbf{U_B} + \dfrac{\tilde{\mathbf{u}}^2}{2}\right] + \nu \Delta \tilde{\mathbf{u}}, \end{cases} \tag{9}$$

where $[\tilde{\mathbf{u}}, \widetilde{\omega}, \tilde{p}]$ are the 3D perturbation fields. Since Eq. (9) is homogeneous along the z-axis, the linear perturbations are taken under the form of normal modes:

$$[\tilde{\mathbf{u}}, \widetilde{\boldsymbol{\omega}}, \tilde{p}](\mathrm{x}, \mathrm{y}, \mathrm{z}, \mathrm{t}) = [\mathbf{u}, \boldsymbol{\omega}, p](\mathrm{x}, \mathrm{y}, \mathrm{t})\, \mathrm{e}^{\mathrm{ikz}} + \mathrm{cc}, \tag{10}$$

where $[\mathbf{u}, \omega, p]$ are the 3D eigenmode. The numerical integration of the linear Navier–Stokes equations is similar to the one described in Section 2.1 except that now the fields $[\mathbf{u}, \omega, p]$ are complex. The 3D eigenmode is expressed in Fourier space:

$$[\mathbf{u}, \boldsymbol{\omega}, p](x, y, t) = \iint [\hat{\mathbf{u}}, \widehat{\boldsymbol{\omega}}, \hat{p}](k_x, k_y, t) * \mathrm{e}^{\mathrm{i}(k_x x + k_y y)}\, \mathrm{dk_x}\, \mathrm{dk_y}. \tag{11}$$

In spectral space, the linearized Navier–Stokes equations, Eq. (9), become:

$$\begin{cases} \mathbf{k_t} \cdot \hat{\mathbf{u}} = 0, \\ \dfrac{\partial \hat{\mathbf{u}}}{\partial t} = P(\mathbf{k_t})\big[\widehat{\mathcal{F}_L}\big] - \nu \mathbf{k_t}^2 \hat{\mathbf{u}} \end{cases} \tag{12}$$

with $P(\mathbf{k_t})$ as defined in the discussion of Eq. (4), $\mathbf{k_t} = (\mathrm{k_x}, \mathrm{k_y}, \mathrm{k})$ and $\mathcal{F}_L = \tilde{\mathbf{u}} \wedge \boldsymbol{\Omega_B} + \mathbf{U_B} \wedge \widetilde{\boldsymbol{\omega}}$.

For this 3D study, the transverse wavenumber k is set during a simulation and the velocity perturbation field is initialized by a solenoidal white noise. All the parameters are similar to that of the basic state computation (Section 2.2). A Krylov method [25] of order $\mathrm{N}=5$ is implemented to compute the five leading eigenmodes. The linearized Navier–Stokes equations, Eq. (9) may be written symbolically as:

$$\frac{\mathrm{d}\tilde{\mathbf{u}}}{\mathrm{dt}}=\underline{\underline{\mathrm{L}}}\tilde{\mathbf{u}}, \tag{13}$$

where $\underline{\underline{\mathrm{L}}}$ is the linear evolution operator. The system, Eq. (13), is integrated over a long period of time until the leading eigenmodes dominate. We save the state vectors at five distinct instants t_j equal to T, $T+\Delta T$, $T+2\Delta T$, $T+3\Delta T$, $T+4\Delta T$ to form the N state vectors $\tilde{\mathbf{u}}_j(x,y,\mathrm{t_j})$ $(j\in[1;N])\}$. Each vector is orthogonalized, using the scalar product associated with the energy, yielding to an orthonormal vector base $\{\mathbf{v}_j(x,y,\mathrm{t_j}),\ j\in[1;N]\}$ spanning a subspace denoted $\mathrm{E_N}$.

The linear evolution operator $\underline{\underline{\mathrm{L}}}$ is then orthogonally projected on the subspace $\mathrm{E_N}$. It becomes $\underline{\underline{\mathrm{L}}}'=\underline{\underline{\mathrm{K}}}^{\mathrm{T}}\,\underline{\underline{\mathrm{L}}}\,\underline{\underline{\mathrm{K}}}$ where $\underline{\underline{\mathrm{K}}}$ is the matrix formed by the base $\{\mathbf{v}_j(x,y,\mathrm{t_j}),\ j\in[1;N]\}$, $\underline{\underline{\mathrm{K}}}^{\mathrm{T}}$ being the tranposed matrix. The 5×5 matrix $\underline{\underline{\mathrm{L}}}'$ is diagonalized giving the eigenvalues σ'_j and the eigenvectors Φ'_j; (σ'_j,Φ'_j) are an approximation of the five leading eigenvalues and eigenvectors (σ_j,Φ_j). The error β_j made on each eigenvalue σ'_j is evaluated by the ratio $\beta_j=\|L\Phi'_j-\lambda_j\Phi'_j\|/\|\Phi'_j\|$.

3.1. Symmetric and antisymmetric modes

Since the primary flow is symmetric under $(x,y,\Omega_B)\to(x+\lambda_{2D}/2,-y,-\Omega_B)$, where λ_{2D} is the period of the basic flow, the 3D secondary instability is characterized by two different modes, where the perturbation fields have distinct symmetry features. These 3D secondary modes are called symmetric and antisymmetric following the work by Robinson and Saffman [26] which refers to the symmetry of the deformations in the streamwise x-direction of the basic vortex tubes (originally aligned with the spanwise z-direction).

The symmetric mode satisfies the relations:

$$\begin{cases}[\mathrm{u_x},\mathrm{u_y},\mathrm{u_z}](\mathrm{x},\mathrm{y},\mathrm{t})=[\mathrm{u_x},-\mathrm{u_y},\mathrm{u_z}](\mathrm{x}+\lambda_{2\mathrm{D}}/2,-\mathrm{y},\mathrm{t}),\\ [\omega_{\mathrm{x}},\omega_{\mathrm{y}},\omega_{\mathrm{z}}](\mathrm{x},\mathrm{y},\mathrm{t})=[-\omega_{\mathrm{x}},\omega_{\mathrm{y}},-\omega_{\mathrm{z}}](\mathrm{x}+\lambda_{2\mathrm{D}}/2,-\mathrm{y},\mathrm{t})\end{cases} \tag{14}$$

and the antisymmetric mode

$$\begin{cases}[\mathrm{u_x},\mathrm{u_y},\mathrm{u_z}](\mathrm{x},\mathrm{y},\mathrm{t})=[-\mathrm{u_x},\mathrm{u_y},-\mathrm{u_z}](\mathrm{x}+\lambda_{2\mathrm{D}}/2,-\mathrm{y},\mathrm{t}),\\ [\omega_{\mathrm{x}},\omega_{\mathrm{y}},\omega_{\mathrm{z}}](x,y,t)=[\omega_{\mathrm{x}},-\omega_{\mathrm{y}},\omega_{\mathrm{z}}](x+\lambda_{2\mathrm{D}}/2,-y,t).\end{cases} \tag{15}$$

Any initial perturbation decompose into symmetric and antisymmetric parts. Two sets of simulations was then performed for each family, the symmetric and antisymmetric one, the symmetries being imposed on the initial conditions.

Because of the invariance of the basic flow $\mathbf{U}_B$ with respect to translation in the z-direction, all the eigenmodes are defined to an arbitrary phase $\mathrm{e}^{\mathrm{i}\phi}$. Furthermore, because of the symmetry of the basic flow previously described, all the stationary modes (σ real with σ the eigenvalue) are associated with an eigenmode with u_x and u_y imaginary and u_z real. In other words, u_z and u_y are respectively in quadrature and in phase with u_x. In terms of vorticity, this means that ω_z is real and ω_x and ω_y are imaginary (in quadrature). For propagative modes (i.e., σ complex) the symmetry imposes that the complex conjugate of σ is also solution. Therefore, if the von Kármán street loses its stability with respect to a wave propagating in the positive z-direction it also loses its stability with respect to the symmetric of this wave, propagating in the negative z-direction.

3.1.1. Growth rate curves

Even though we obtained the five leading eigenmodes by the fifth order Krylov method, we will focus in the present analysis to the significantly unstable branches. The development and implementation of the fifth order method gives a better accuracy on the first three leading modes. Figs. 2 and 3 show the growth rate curves of the most amplified modes (a) and their frequencies when they are propagative (b), as a function of k, for the symmetric and antisymmetric modes respectively. The stationary modes ($\sigma\in\mathbb{R}$) are indicated by a plus and the propagative modes ($\sigma\in\mathbb{C}$) by a circle.

For symmetric modes, for wavenumbers $k\leqslant 0.20$, all modes are stable. In the range $[0.20, 0.52]$, propagative modes are dominant. The stationary mode which is stable for $k\leqslant 0.20$, becomes dominant for $k\geqslant 0.52$. The propagative branch shows two local maxima, at $k=0.4$ with $\sigma_{r_{\max}}=0.036$ and at $k=0.85$ with $\sigma_{r_{\max}}=0.044$ and a cutoff value $k_c\simeq 1.5$. The maximum growth rate is achieved for the stationary mode, denotes SI on Fig. 2(a), close to $k\simeq 1.2$ with $\sigma_{r_{\max}}=0.078$. For $k\geqslant 1.2$, the growth rate decreases monotically with the wavenumber k and vanishes at the cutoff wavenumber $k_c\simeq 2.8$. This damping is, as we will argue in the following section, the manifestation of viscous effects that become dominant when the wavenumber k increases.

For the antisymmetric modes, we see on Fig. 3(a) that two amplified stationary branches exist in the range $[0, 0.12]$. These two stationary branches pinch at $k=0.12$ and give rise to two propagative branches, which become stable for $k\geqslant 0.39$. A third stationary branch, referred to as ASI on Fig. 3(a), is unstable in the range $k\in[0.38, 2.8]$. The most unstable wavenumber is in this branch close to $k=1.2$ and the growth rate is slightly higher than the symmetric counterpart with $\sigma_{r_{\max}}=0.088$. The cutoff wavenumber corresponding to the stabilization of the mode is the same as in the symmetric case, i.e., $k_c=2.8$.

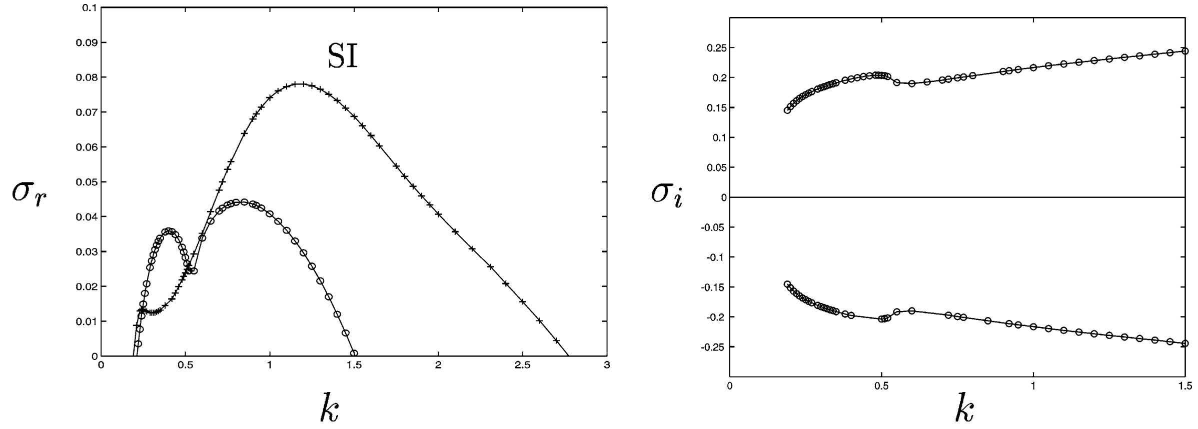

(a) (b)

Fig. 2. (a) Growth rate σ_r of the unstable symmetric modes as a function of the wavenumber k. (b) Their frequencies σ_i which are nonzero only when the modes are propagative.

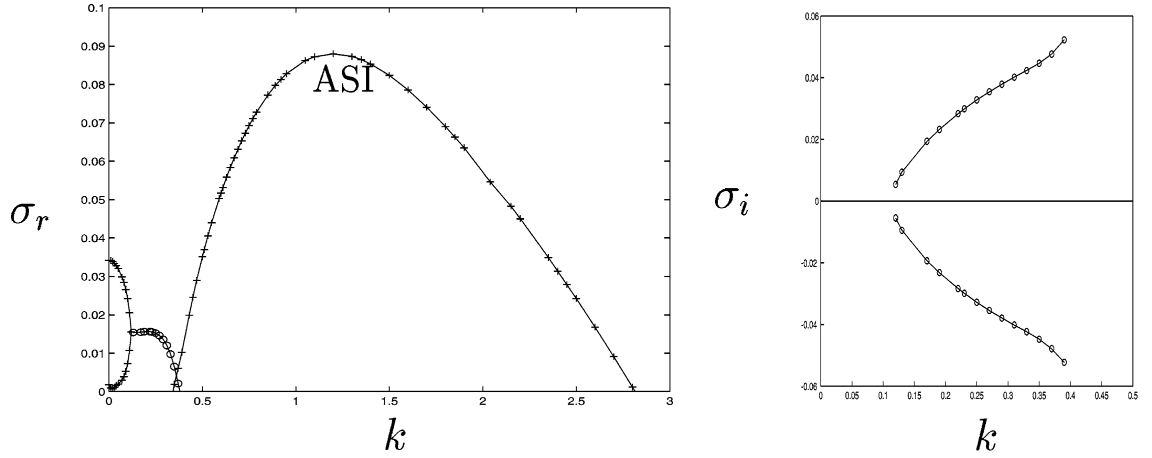

(a) (b)

Fig. 3. (a) Growth rate σ_r of the leading antisymmetric modes as a function of the wavenumber k. (b) Their frequencies σ_i when they are propagative and unstable.

3.1.2. Eigenmode structure for the SI branch

The previous section showed that the most unstable mode is stationary. The symmetric and antisymmetric modes behave similarly. A detailed mode structure shows that both the SI and ASI modes present similar features. We restrict therefore the analysis of the perturbation field to the symmetric mode SI. Figs. 4(a) and 4(b) show the perturbation in the spanwise vorticity field ω_z, corresponding to the eigenmode at $k = 1.2$ and $k = 2.2$ on the SI branch. Figs. 4(c) and 4(d) show the corresponding total perturbation enstrophy field $|\omega| = |\omega_x|^2 + |\omega_y|^2 + |\omega_z|^2$. Because of the symmetry properties of the stationary mode, ω_z is a real field, whereas ω_x and ω_y are imaginary fields. For $k = 1.2$, the spanwise vorticity field (Fig. 4(a)) exhibits the characteristic dipole structure of the first stationary elliptic mode described by Pierrehumbert [27]. At $k = 2.2$, the spanwise vorticity field is still in the core of the primary vortices, its structure is multipolar (Fig. 4(b)) but the link with higher order elliptic modes is only indicative. The total enstrophy fields (Fig. 4 (c) and (d)) show that the higher the wavenumber k the more the perturbation is concentrated in the braid region on the stretched manifold of the stationary hyperbolic point. At $k = 1.2$, the core of the primary vortices contributes to the total enstrophy, whereas, at $k = 2.2$, the perturbation is one order of magnitude smaller in the core. The ω_z field is in this case one order of magnitude smaller than the other field and one may imagine that this is the reason why the spatial distribution is far from the elliptic instability prediction. At $k = 1.2$, the amplitude of the perturbation in the core is only two times smaller than in the braid and when k increases, the core contribution fades away.

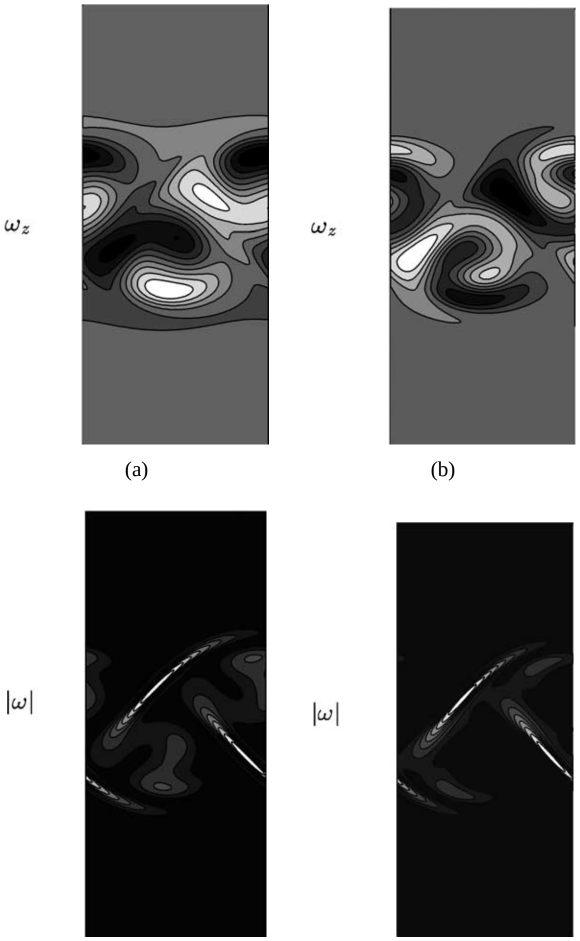

(a) (b)

(c) (d)

Fig. 4. Transverse vorticity field w_z of Mode SI. (a) $k = 1.2$, (b) $k = 2.2$. Isocontours are equally spaced. Dark corresponds to negative values of the vorticity ω_z and white colors to positive values. Local enstrophy $|\omega|$ of the stationary mode SI. (c) $k = 1.2$, (d) $k = 2.2$. Enstrophy maxima are in white and in black the enstrophy vanishes. Isocontours are equally spaced.

4. Discussion

4.1. Comparison with local elliptic and hyperbolic theories

The maximum growth rate, the wavenumber, at which it occurs, and the associated spanwise vorticity fields are in agreement with the elliptic instability theories, local analysis of Pierrehumbert [27] and asymptotic global analysis Bayly [28], and plug vortex computation of Tsai and Widnall [29], that all predict a maximum growth rate close to 9/16 of the strain rate ε_B at the point of maximum vorticity marked by a triangle on Fig. 1(c). The theoretical growth rate value for the elliptic instability is 0.08 which is in agreement with the computed values of 0.078 and 0.088. Similarly Landman and Saffman [30] obtained a viscous cutoff for the elliptic instability that predicts a wavenumber value of 2.5 quite comparable with the value of $k_c = 2.8$ presently computed. In comparison, the growth rate predicted by the local hyperbolic instability (Caulfield and Kerswell [12]) is equal the 0.47 value of the field Δ at the hyperbolic point marked by a star on Fig. 1(c). The value predicted by hyperbolic instability is more than five times larger than the computed maximum growth rate 0.078 or 0.088. Similarly, the cutoff wavenumber is $k = 6$ which is two times larger that the computed one $k_c = 2.8$.

As already commented, identification of an elliptic instability of the vortex core is confirmed by the transverse vorticity perturbation field ω_z at $k = 1.2$ (Fig. 4(a)) that exhibits the characteristic dipole structure of the first stationary elliptic mode described by Pierrehumbert [27]. At higher wavenumbers, the transverse vorticity perturbation field keeps a structure coherent with the elliptic instability, but the longitudinal vorticity perturbation becomes up to ten times more intense and gets localized in the positive stretching direction of the hyperbolic point. This expresses the tendency to form longitudinal vortices in the braid region. But at this high wavenumber the growth rate is still determined by the elliptic instability and not by the hyperbolic instability. This paradoxical result indicates that the hyperbolic region is "slaved" to the elliptic region: it amplifies the perturbation but does not affect the growth rate. Thompson et al. [31] draw a similar conclusion; elliptic instability is dominant for the maintenance of the Mode A instability in the wake of a circular cylinder. This is coherent with the recent paper by Caulfield and Kerswell [12] on the nonnormality of the linearized Navier–Stokes evolution operator and transient growth in shear flows. Finite size hyperbolic regions are responsible for intense transient growth but cannot sustain long time perturbation energy growth. On the contrary, since particle paths are closed in elliptic region, the local or short time instability stands for ever and imposes long time energy growth and therefore positive global growth rate.

4.2. *Comparison with the experiments*

Julien et al. [20] have experimentally studied the wake of thin flat plate. The primary 2D instability was forced by modulating the lower layer flow rate in order to regularize the von Kármán street in space and time. They showed in particular that the symmetric and the antisymmetric modes have similar growth rates, both selecting a wavenumber close to unity, when nondimensionalized by the von Kármán street periodicity. By forcing the 3D symmetric mode they were able to estimate both the maximum spatial growth rate 0.38 cm^{-1} and the corresponding maximum nondimensionalized wavenumber $\lambda_{2D}/\lambda_{3D} = 1.3$. These results are in remarkable agreement with the present computation since both modes have a maximum wavenumber close to 1.2. For growth rate comparisons, the spatial growth rate has to be transformed into a temporal growth rate using the Gaster transformation (Huerre and Monkewitz [32]) that requires the knowledge of the group velocity. Here we estimate the group velocity of the 3D perturbations by the velocity of the primary vortices since the present numerical analysis shows that the instability is stationary in the frame moving with the vortices. In the experiment, this velocity is about 0.85 times the fluid velocity ($\overline{U} = 6.3\ \mathrm{cm\cdot s^{-1}}$) and, therefore, the dimensional experimental temporal growth rate is $\sigma_{\max}^{\exp} = 1.9\ \mathrm{s}^{-1}$ that gives a nondimensionalized growth rate $\sigma_{\max} = \delta_w \sigma_{\max}^{\exp}/(0.8\overline{U})$ 0.8 being the defect velocity in the experiments and $\delta_w = 0.35$ cm the thickness of the wake. This adimensionalized experimental estimate, $\sigma_{\max} = 0.13$, of the maximum growth rate measured experimentally is of the same order of magnitude but three time larger than the one we compute $\delta\sigma_{r_{\max}}/\Delta U = 0.08/(2(\sinh^{-} 1(1))) = 0.04$. This discrepancy in growth rate may be due to the weakening of the instability once the wake is formed, as already observed by Sutherland and Peltier [19].

5. Conclusion

The agreement between experiments and stability analysis of a streamwise periodic wake favours the idea that local mechanisms rule the secondary instability of a flat plat wake (or more generally slender body wake). The leading mechanism is the elliptic instability of the vortex cores for both symmetric and antisymmetric modes. It sets the maximum growth rate and wavenumber cutoff. The hyperbolic point plays a subtle role in amplifying perturbations in a transient way. When triggered by the elliptic instability of the vortex cores, the hyperbolic instability intensifies the perturbations resulting in the formation of intense longitudinal vorticity. Longitudinal vorticity field is the most intense component of the eigenmode and is concentrated in the stretching direction of the hyperbolic point but the growth rate is predicted by the elliptic instability of the vortex cores.

References

[1] P.G. Drazin, W.H. Reid, Hydrodynamic Stability, Cambridge University Press, 1981.
[2] F.K. Browand, T.R. Troutt, A note on the spanwise structure in the two-dimensional mixing layer, J. Fluid Mech. 97 (1980) 771.
[3] R. Breidenthal, Structure in turbulent mixing layers and wakes using a chemical reaction, J. Fluid Mech. 109 (1981) 1.
[4] J. Jimenez, On the visual growth of the turbulent mixing layer, J. Fluid Mech. 96 (1980) 447.
[5] Bernal, Roshko, Streamwise vortex structure in plane mixing layers, J. Fluid Mech. 170 (1986) 499.
[6] A.J. Yule, Large-scale structure in the mixing-layer of a round jet, J. Fluid Mech. 89 (1978) 413.
[7] P.A. Monkewitz, D.W. Bechert, B. Barsikow, B. Lehmann, Self-excited oscillations and mixing in a heated round jet, J. Fluid Mech. 213 (1990) 611.
[8] E. Meiburg, J.C. Lasheras, Experimental and numerical investigation of the three-dimensional transition in plane wakes, J. Fluid Mech. 190 (1987) 1.
[9] C.H.K. Williamson, Three-dimensional wake transition, J. Fluid Mech. 328 (1994) 345.
[10] C.H.K. Williamson, Vortex dynamics in the cylinder wake, Annu. Rev. Fluid Mech. 28 (1996) 477.
[11] T. Leweke, C.H.K. Williamson, Three-dimensional instabilities in wake transition, Eur. J. Mech. B Fluids 17 (4) (1998) 571.
[12] C.P. Caulfield, R.R. Kerswell, The nonlinear development of three-dimensional disturbances at hyperbolic stagnation points: a model of the braid region in mixing layers, Phys. Fluids 12 (5) (2000) 1032.

[13] R.R. Kerswell, Elliptical instability, Annu. Rev. Fluid Mech. 34 (2002) 1.
[14] R.T. Pierrehumbert, S.E. Widnall, The two- and three-dimensional instabilities of a spatially periodic shear layer, J. Fluid Mech. 114 (1982) 59.
[15] J.T. Stuart, On finite amplitude oscillations in laminar mixing layers, J. Fluid Mech. 29 (1967) 417.
[16] G.P. Klaassen, W.R. Peltier, The influence of stratification on secondary instability in free shear layers, J. Fluid Mech. 227 (1991) 71.
[17] P.G. Potylitsin, W.R. Peltier, Three-dimensional destabilization of Stuart vortices: the influence of rotation and ellipticity, J. Fluid Mech. 387 (1999) 205.
[18] C.P. Caulfield, W.R. Peltier, The anatomy of the mixing transition in homogeneous and stratified free shear layers, J. Fluid Mech. 413 (2000) 1.
[19] B.R. Sutherland, W.R. Peltier, Turbulence transition and internal wave generation in density stratified jets, Phys. Fluids 6 (1994) 1267.
[20] S. Julien, J.C. Lasheras, J.-M. Chomaz, Three-dimensional instability and vorticity patterns in the wake of a flat plate, J. Fluid Mech. 479 (2003) 155.
[21] D. Barkley, R.D. Henderson, Three-dimensional Floquet stability analysis of the wake of a circular cylinder, J. Fluid Mech. 322 (1996) 215.
[22] P. Brancher, J.-M. Chomaz, P. Huerre, Direct numerical simulations of round jets: vortex induction and side-jets, Phys. Fluids 6 (5) (1994) 1768; Phys. Rev. Lett. 57 (1986) 2160.
[23] P.G. Drazin, L.N. Howard, Hydrodynamic stability of parallel flow of inviscid fluid, in: G. Kuerti (Ed.), Adv. in Appl. Mech., Vol. 7, Academic Press, New York, 1966.
[24] P.A. Monkewitz, The absolute and convective nature of instability in two-dimensional wakes at low Reynolds numbers, Phys. Fluids 31 (1988) 999.
[25] W.S. Edwards, L.S. Tuckerman, R.A. Friesner, D.C. Sorensen, Krylov methods for the incompressible Navier–Stokes equations, J. Comput. Phys. 110 (1994) 82.
[26] A.C. Robinson, P.G. Saffman, Three-dimensional stability of vortex arrays, J. Fluid Mech. 125 (1982) 411.
[27] R.T. Pierrehumbert, Universal short-wave instability of two-dimensional eddies in an inviscid fluid, Phys. Rev. Lett. 57 (1986) 2157.
[28] B.J. Bayly, Three-dimensional instability of elliptical flow, Phys. Rev. Lett. 57 (1986) 2160.
[29] C.-Y. Tsai, S.E. Widnall, The stability of short waves on a straight vortex filament in a weak externally imposed strain field, J. Fluid Mech. 73 (1976) 721.
[30] M.J. Landman, P.G. Saffman, The three-dimensional instability of strained vortices in a viscous fluid, Phys. Fluids 30 (1987) 2339.
[31] M.C. Thompson, T. Leweke, C.H.K. Williamson, The physical mechanism of transition in bluff body wakes, J. Fluids Structures 15 (2001) 607.
[32] P. Huerre, P. Monkewitz, Local and global instabilities in spatially developing flows, Annu. Rev. Fluid Mech. 22 (1990) 473.